# A polarized multispectral imaging system for quantitative assessment of hypertrophic scars

**Pejhman Ghassemi,[1,2] Taryn E. Travis,[2] Lauren T. Moffatt,[2] Jeffrey W. Shupp,[2,3] and Jessica C. Ramella-Roman[3,4,*]**

[1]*Department of Electrical Engineering, The Catholic University of America, 620 Michigan Avenue, NE, Washington, DC 20064, USA*
[2]*Medstar Health Research Institute, MedStar Washington Hospital Center, 108 Irving Street, NW, Washington, DC 20010, USA*
[3]*Department of Biomedical Engineering, The Catholic University of America, 620 Michigan Avenue, NE, Washington, DC 20064, USA*
[4]*Department of Biomedical Engineering and Herbert Wertheim College of Medicine, Florida International University, 10555 W. Flagler Street, Miami, FL 33174, USA*
[*]*jramella@fiu.edu*

**Abstract:** Hypertrophic scars (HTS) are a pathologic reaction of the skin and soft tissue to burn or other traumatic injury. Scar tissue can cause patients serious functional and cosmetic issues. Scar management strategies, specifically scar assessment techniques, are vital to improve clinical outcome. To date, no entirely objective method for scar assessment has been embraced by the medical community. In this study, we introduce for the first time, a novel polarized multispectral imaging system combining out-of-plane Stokes polarimetry and Spatial Frequency Domain Imaging (SFDI). This imaging system enables us to assess the pathophysiology (hemoglobin, blood oxygenation, water, and melanin) and structural features (cellularity and roughness) of HTS. To apply the proposed technique in an *in vivo* experiment, dermal wounds were created in a porcine model and allowed to form into scars. The developed scars were then measured at various time points using the imaging system. Results showed a good agreement with clinical Vancouver Scar Scale assessment and histological examinations.

©2014 Optical Society of America

OCIS codes: (110.0110) Imaging systems; (110.4234) Multispectral and hyperspectral imaging.

## References and links

1. H. A. Linares, "From wound to scar," Burns **22**(5), 339–352 (1996).
2. M. A. Hardy, "The biology of scar formation," Phys. Ther. **69**(12), 1014–1024 (1989).
3. D. Wolfram, A. Tzankov, P. Pülzl, and H. Piza-Katzer, "Hypertrophic scars and keloids - A review of their pathophysiology, risk factors, and therapeutic management," Dermatol. Surg. **35**(2), 171–181 (2009).
4. J. E. Dunphy and D. S. Jackson, "Practical applications of experimental studies in the care of te primarily closed wound," Am. J. Surg. **104**(2), 273–282 (1962).
5. K. M. Bombaro, L. H. Engrav, G. J. Carrougher, S. A. Wiechman, L. Faucher, B. A. Costa, D. M. Heimbach, F. P. Rivara, and S. Honari, "What is the prevalence of hypertrophic scarring following burns?" Burns **29**(4), 299–302 (2003).
6. R. Robert, W. Meyer, S. Bishop, L. Rosenberg, L. Murphy, and P. Blakeney, "Disfiguring burn scars and adolescent self-esteem," Burns **25**(7), 581–585 (1999).
7. T. Sullivan, J. Smith, J. Kermode, E. McIver, and D. J. Courtemanche, "Rating the burn scar," J. Burn Care Rehabil. **11**(3), 256–260 (1990).
8. M. J. Baryza and G. A. Baryza, "The Vancouver scar scale: an administration tool and its interrater reliability," J. Burn Care Rehabil. **16**(5), 535–538 (1995).
9. R. Fearmonti, J. Bond, D. Erdmann, and H. Levinson, "A review of scar scales and scar measuring devices," Eplasty **10**, e43 (2010).
10. R. Richard, M. J. Baryza, J. A. Carr, W. S. Dewey, M. E. Dougherty, L. Forbes-Duchart, B. J. Franzen, T. Healey, M. E. Lester, S. K. Li, M. Moore, D. Nakamura, B. Nedelec, J. Niszczak, I. S. Parry, C. D. Quick, M.

Serghiou, R. S. Ward, L. Ware, and A. Young, "Burn rehabilitation and research: proceedings of a consensus summit," J. Burn Care Res. **30**(4), 543–573 (2009).

11. H. Khorasani, Z. Zheng, C. Nguyen, J. Zara, X. Zhang, J. Wang, K. Ting, and C. Soo, "A quantitative approach to scar analysis," Am. J. Pathol. **178**(2), 621–628 (2011).
12. M. C. Pierce, J. Strasswimmer, B. H. Park, B. Cense, and J. F. de Boer, "Advances in optical coherence tomography imaging for dermatology," J. Invest. Dermatol. **123**(3), 458–463 (2004).
13. M. Wolman and T. Gillman, "A polarized light study of collagen in dermal wound healing," Br. J. Exp. Pathol. **53**(2), 85–89 (1972).
14. S. L. Jacques, J. C. Ramella-Roman, and K. Lee, "Imaging skin pathology with polarized light," J. Biomed. Opt. **7**(3), 329–340 (2002).
15. A. G. Ferdman and I. V. Yannas, "Scattering of light from histologic sections: a new method for the analysis of connective tissue," J. Invest. Dermatol. **100**(5), 710–716 (1993).
16. V. Da Costa, R. Wei, R. Lim, C. H. Sun, J. J. Brown, and B. J. Wong, "Nondestructive imaging of live human keloid and facial tissue using multiphoton microscopy," Arch. Facial Plast. Surg. **10**(1), 38–43 (2008).
17. G. Chen, J. Chen, S. Zhuo, S. Xiong, H. Zeng, X. Jiang, R. Chen, and S. Xie, "Nonlinear spectral imaging of human hypertrophic scar based on two-photon excited fluorescence and second-harmonic generation," Br. J. Dermatol. **161**(1), 48–55 (2009).
18. B. A. Torkian, A. T. Yeh, R. Engel, C. H. Sun, B. J. Tromberg, and B. J. Wong, "Modeling aberrant wound healing using tissue-engineered skin constructs and multiphoton microscopy," Arch. Facial Plast. Surg. **6**(3), 180–187 (2004).
19. X. Zhu, S. Zhuo, L. Zheng, K. Lu, X. Jiang, J. Chen, and B. Lin, "Quantified characterization of human cutaneous normal scar using multiphoton microscopy," J. Biophotonics **3**(1-2), 108–116 (2010).
20. X. Zhu, S. Zhuo, L. Zheng, X. Jiang, J. Chen, and B. Lin, "Quantification of scar margin in keloid different from atrophic scar by multiphoton microscopic imaging," Scanning **33**(4), 195–200 (2011).
21. N. Kurokawa, K. Ueda, and M. Tsuji, "Study of microvascular structure in keloid and hypertrophic scars: density of microvessels and the efficacy of three-dimensional vascular imaging," J. Plast. Surg. Hand Surg. **44**(6), 272–277 (2010).
22. I. S. Kaartinen, P. O. Välisuo, J. T. Alander, and H. O. Kuokkanen, "Objective scar assessment--a new method using standardized digital imaging and spectral modelling," Burns **37**(1), 74–81 (2011).
23. I. S. Kaartinen, P. O. Va Lisuo, V. Bochko, J. T. Alander, and H. O. Kuokkanen, "How to assess scar hypertrophy-a comparison of subjective scales and spectrocutometry: a new objective method," Wound Rep. Reg. **19**(3), 316–323 (2011).
24. L. J. Draaijers, F. R. Tempelman, Y. A. Botman, R. W. Kreis, E. Middelkoop, and P. P. van Zuijlen, "Colour evaluation in scars: tristimulus colorimeter, narrow-band simple reflectance meter or subjective evaluation?" Burns **30**(2), 103–107 (2004).
25. R. Bray, K. Forrester, C. Leonard, R. McArthur, J. Tulip, and R. Lindsay, "Laser Doppler imaging of burn scars: a comparison of wavelength and scanning methods," Burns **29**(3), 199–206 (2003).
26. C. J. Stewart, R. Frank, K. R. Forrester, J. Tulip, R. Lindsay, and R. C. Bray, "A comparison of two laser-based methods for determination of burn scar perfusion: laser Doppler versus laser speckle imaging," Burns **31**(6), 744–752 (2005).
27. M. C. Bloemen, M. S. van Gerven, M. B. van der Wal, P. D. Verhaegen, and E. Middelkoop, "An objective device for measuring surface roughness of skin and scars," J. Am. Acad. Dermatol. **64**(4), 706–715 (2011).
28. E. K. Yeong, R. Mann, L. H. Engrav, M. Goldberg, V. Cain, B. Costa, M. Moore, D. Nakamura, and J. Lee, "Improved burn scar assessment with use of a new scar-rating scale," J. Burn Care Rehabil. **18**(4), 353–355 (1997).
29. S. Aarabi, K. A. Bhatt, Y. Shi, J. Paterno, E. I. Chang, S. A. Loh, J. W. Holmes, M. T. Longaker, H. Yee, and G. C. Gurtner, "Mechanical load initiates hypertrophic scar formation through decreased cellular apoptosis," FASEB J. **21**(12), 3250–3261 (2007).
30. C. C. Yates, P. Krishna, D. Whaley, R. Bodnar, T. Turner, and A. Wells, "Lack of CXC chemokine receptor 3 signaling leads to hypertrophic and hypercellular scarring," Am. J. Pathol. **176**(4), 1743–1755 (2010).
31. P. Ghassemi, P. Lemaillet, T. A. Germer, J. W. Shupp, S. S. Venna, M. E. Boisvert, K. E. Flanagan, M. H. Jordan, and J. C. Ramella-Roman, "Out-of-plane Stokes imaging polarimeter for early skin cancer diagnosis," J. Biomed. Opt. **17**(7), 076014 (2012).
32. J. C. Ramella-Roman, B. Boulbry, and T. A. Germer, "Hemispherical imaging of skin with polarized light," in Saratov Fall Meeting, Optical Technologies in Biophysics and Medicine VIII, Valery V. Tuchin, Ed., Proc. SPIE **6535**, 65350U (2006).
33. H. M. Merklinger, *Focusing the View Camera* (Belford, Nova Scotia: Seaboard Printing Ltd. 1996).
34. D. J. Cuccia, F. Bevilacqua, A. J. Durkin, F. R. Ayers, and B. J. Tromberg, "Quantitation and mapping of tissue optical properties using modulated imaging," J. Biomed. Opt. **14**(2), 024012 (2009).
35. J. R. Weber, D. J. Cuccia, A. J. Durkin, and B. J. Tromberg, "Noncontact imaging of absorption and scattering in layered tissue using spatially modulated structured light," J. Appl. Phys. **105**(10), 102028 (2009).
36. J. A. Nelder and R. Mead, "A simplex method for function minimization," Comput. J. **7**(4), 308–313 (1965).
37. X. Ma, J. Q. Lu, H. Ding, and X. H. Hu, "Bulk optical parameters of porcine skin dermis at eight wavelengths from 325 to 1557 nm," Opt. Lett. **30**(4), 412–414 (2005).

38. T. Yu, X. Wen, V. V. Tuchin, Q. Luo, and D. Zhu, "Quantitative analysis of dehydration in porcine skin for assessing mechanism of optical clearing," J. Biomed. Opt. **16**(9), 095002 (2011).
39. R. B. Saager, D. J. Cuccia, S. Saggese, K. M. Kelly, and A. J. Durkin, "A light emitting diode (LED) based spatial frequency domain imaging system for nonmelanoma skin cancer: quantitative reflectance imaging," Lasers Surg. Med. **45**(4), 207–215 (2013).
40. A. M. Laughney, V. Krishnaswamy, T. B. Rice, D. J. Cuccia, R. J. Barth, B. J. Tromberg, K. D. Paulsen, B. W. Pogue, and W. A. Wells, "System analysis of spatial frequency domain imaging for quantitative mapping of surgically resected breast tissues," J. Biomed. Opt. **18**(3), 036012 (2013).
41. B. Boulbry, J. C. Ramella-Roman, and T. A. Germer, "Self-consistent calibration of a spectro-ellipsometer using a Fresnel rhomb as a reference sample," Appl. Opt. **46**(35), 8533–8541 (2007).
42. T. A. Germer and C. C. Asmail, "Bidirectional ellipsometry and its application to the characterization of surfaces," Polarization: Measurement, Analysis, and Remote Sensing, Proc. SPIE **3121**, 173–182 (1997).
43. T. A. Germer, "SCATMECH: Polarized Light Scattering C++ Class Library," (2008), *http://physics.nist.gov/scatmech*.
44. T. Moffitt, Y. C. Chen, and S. A. Prahl, "Preparation and characterization of polyurethane optical phantoms," J. Biomed. Opt. **11**(4), 041103 (2006).
45. M. L. Ramos, A. Gragnani, and L. M. Ferreira, "Is there an ideal animal model to study hypertrophic scarring?" J. Burn Care Res. **29**(2), 363–368 (2008).
46. R. Tsou, J. K. Cole, A. B. Nathens, F. F. Isik, D. M. Heimbach, L. H. Engrav, and N. S. Gibran, "Analysis of hypertrophic and normal scar gene expression with cDNA microarrays," J. Burn Care Rehabil. **21**(6), 541–550 (2000).
47. Z. Liang, L. H. Engrav, P. Muangman, L. A. Muffley, K. Q. Zhu, G. J. Carrougher, R. A. Underwood, and N. S. Gibran, "Nerve quantification in female red Duroc pig (FRDP) scar compared to human hypertrophic scar," Burns **30**(1), 57–64 (2004).
48. N. Harunari, K. Q. Zhu, R. T. Armendariz, H. Deubner, P. Muangman, G. J. Carrougher, F. F. Isik, N. S. Gibran, and L. H. Engrav, "Histology of the thick scar on the female, red Duroc pig: final similarities to human hypertrophic scar," Burns **32**(6), 669–677 (2006).
49. Y. Xie, K. Q. Zhu, H. Deubner, D. A. Emerson, G. J. Carrougher, N. S. Gibran, and L. H. Engrav, "The microvasculature in cutaneous wound healing in the female red Duroc pig is similar to that in human hypertrophic scars and different from that in the female yorkshire pig," J. Burn Care Res. **28**(3), 500–506 (2007).
50. K. Q. Zhu, G. J. Carrougher, O. P. Couture, C. K. Tuggle, N. S. Gibran, and L. H. Engrav, "Expression of collagen genes in the cones of skin in the Duroc/Yorkshire porcine model of fibroproliferative scarring," J. Burn Care Res. **29**(5), 815–827 (2008).
51. T. E. Travis, M. J. Mino, L. T. Moffatt, N. A. Mauskar, N. J. Prindeze, P. Ghassemi, J. C. Ramella-Roman, M. H. Jordan, and J. W. Shupp, "Biphasic presence of fibrocytes in a porcine hypertrophic scar model," J. Burn Care Res. **34**(2), S94 (2014).
52. D. F. Sloan, R. D. Brown, C. H. Wells, and J. G. Hilton, "Tissue gases in human hypertrophic burn scars," Plast. Reconstr. Surg. **61**(3), 431–436 (1978).
53. S. Ichioka, T. Ando, M. Shibata, N. Sekiya, and T. Nakatsuka, "Oxygen consumption of keloids and hypertrophic scars," Ann. Plast. Surg. **60**(2), 194–197 (2008).
54. M. L. Stoner and F. M. Wood, "The treatment of hypopigmented lesions with cultured epithelial autograft," J. Burn Care Rehabil. **21**(1), 50–54 (2000).
55. T. E. Travis, P. Ghassemi, N. J. Priendez, D. W. Paul, L. T. Moffatt, J. C. Ramella-Roman, M. H. Jordan, and J. W. Shupp, "Histological and optical characteristics of pigmented scars in a swine model of human wound healing," Abstract. Proceedings of the American Burn Association **46**, 104 (2014).
56. P. Gong, R. A. McLaughlin, Y. M. Liew, P. R. Munro, F. M. Wood, and D. D. Sampson, "Assessment of human burn scars with optical coherence tomography by imaging the attenuation coefficient of tissue after vascular masking," J. Biomed. Opt. **19**(2), 021111 (2014).
57. E. E. Tredget, B. Nedelec, P. G. Scott, and A. Ghahary, "Hypertrophic scars, keloids, and contractures. The cellular and molecular basis for therapy," Surg. Clin. North Am. **77**(3), 701–730 (1997).
58. N. Bodenschatz, A. Brandes, A. Liemert, and A. Kienle, "Sources of errors in spatial frequency domain imaging of scattering media," J. Biomed. Opt. **19**(7), 071405 (2014), doi:10.1117/1.JBO.19.7.071405.
59. A. C. Vivas, J. C. Tang, A. D. Maderal, and M. H. Viera, "Hypertrophic scars and keloids, part 1: convensional treatments," Cosmet. Dermatol. **25**(7), 309–316 (2012).

## 1. Introduction

A scar is an aberrant response to injury such as trauma, surgery, or burn. The normal balance of collagen synthesis and degradation seen in uninjured skin appear to be disrupted in scar formation, as is the normal ratio of collagen I/III [1]. Thus, the processes of fibrosis and scar formation do not appear to regenerate skin and soft tissue similarly to the homeostasis maintained uninjured skin. Scar therapies aim to prevent the pathologic characteristics of fibrosis and when already formed, to treat these issues, making scar more similar to uninjured skin. Knowledge of the biology and processes of normal wound healing is important to

understand and target the pathologic mechanisms of scars. Wound healing is generally thought of in three separate phases: 1) inflammatory, 2) fibroproliferative, and 3) remodeling [2–4] (Fig. 1). Scar formation generally begins during the fibroproliferative phase of wound healing with further maturation occurring during the remodeling phase.
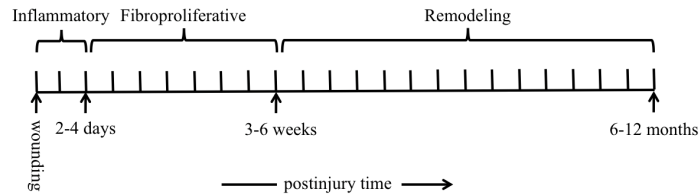


Fig. 1. The process of wound healing vs. postinjury time.

Despite ongoing research, hypertrophic scars are still relatively poorly understood and continue to be a devastating morbidity following injury, particularly thermal trauma. Their prevalence following burn injury is reported to be as high as 67% [5]. When scar forms contracture, it often leads to significant impairment in function and inhibits patients from returning to work, participating in leisure activities, and may even render them less able to care for themselves. Additionally, patients with hypertrophic scars can suffer great psychosocial setbacks due to their disfigured appearances [6].

Scars are commonly evaluated by clinicians using the Vancouver Scar Scale (VSS). The VSS, though imperfect, is one of the most widely used clinical scar assessment tools. It was introduced in the nineties and relies on a clinician's subjective evaluation of scar pliability, height, vascularity, and pigmentation [7,8]. Other scaling protocols exist and are used to subjectively characterize scars [9]. The Visual Analog Scale (VAS) is a photo-based scale which includes many of the parameters of the VSS in addition to contour and observer acceptability. The Patient and Observer Scar Assessment Scale (POSAS) incorporates patient symptoms of pain and pruritus as well as information captured by the VSS. The Manchester Scar Scale (MSS) assesses additional parameters including texture, skin margins, and size. Finally, the Stony Brook Scar Evaluation Scale (SBSES) which is specifically designed to assess short-term wound repair outcomes, evaluates parameters such as width, height, color, and appearance of suture or staple marks.

While there are a multitude of subjective scales to assess and catalog wound and scar quality, there remains a continued need for more reliable, objective techniques to diagnose and qualify scar development. This is underscored by the fact that greater than 30% of the respondents to a survey by the American Burn Association's Rehabilitation Committee regarding pertinent research needs in burn care indicated that scar management was a high priority [10]. Several investigative groups have been developing innovative scar evaluation techniques; Khorasani *et al* have used confocal microscopy for scar indexing based on collagen structure [11]. Pierce *et al* have developed an optical coherence tomography (OCT)-based system to study collagen structure, birefringence, and blood flow in scars [12]. Other groups have applied polarization-sensitive methods to perform collagen architectural analysis and scar imaging [13,14]. Other objective methods, such as laser scattering and multi-photon microscopy, have been described as tools for studying the orientation and alignment of collagen fibers [15–20]. Digital imaging is applied to measure concentration change of hemoglobin and melanin, and also 3D reconstruction of vascular pattern in scared tissue [21–23]. Draaijers *et al* used spectral reflectance to measure the degree of vascularity and pigmentation of scars [24]. Laser Doppler imaging (LDI) and laser speckle imaging have also been employed for scar blood perfusion assessment [25,26]. Finally Bloemen et al. [27] devised a method to monitor surface roughness in skin and applied it to the study of wrinkles and scars.

The ultimate goal of this work was to develop an imaging system to quantify scar quality based on the relatively similar metrics used in the VSS as well as newer scales [28–30]. The device consists of a polarized multispectral imaging apparatus combining out-of-plane Stokes polarimetry and Spatial Frequency Domain Imaging (SFDI). An off-the-shelf LDI system supplemented the imaging techniques used in this study. As shown in Table 1 with one system we are able to monitor several of the metrics of interest, and we believe ours is the first system capable to do so. This newly developed method could ultimately lead to improved characterization, potentially leading to additional treatment options for hypertrophic scar.

**Table 1. Comparison between optical methods of scar assessment and this study.**

| | Scar parameters | Other investigators | This work |
|---|---|---|---|
| VSS | Vascularity/Blood perfusion | Pierce *et al* [12], OCT; Kurokawa *et al* [21], Kaartinen *et al* [22,23], Digital imaging; Draaijers *et al* [24], Spectral reflectance meter; Bray *et al* [25], Stewart *et al* [26], Laser Doppler imaging and Laser speckle imaging. | Yes |
| | Pigmentation | Draaijers *et al* [24], Spectral reflectance meter. | Yes |
| | Pliability | — | — |
| | Height | — | — |
| other scales | Roughness | Bloemen et al. [27] | Yes |
| | Cellularity | — | Yes |

## 2. Materials and methods

### 2.1 The polarized multispectral imaging system

This novel spectral imaging system was designed based on two different imaging modalities: out-of-plane Stokes polarimetry and SFDI (The first generation of the Stokes polarimeter was introduced in [31].). All components of the polarized multispectral imaging system were positioned around a custom-machined hemispherical shell, which was connected to a supporting structure via an adjustable arm. The hemispherical shell provided multi-angle out-of-plane measurements without the use of moving parts, and acted as a support for components of the imaging arm as well as SFDI light projection components. Figure 2 illustrates a side-view of the system geometry, showing an illumination tube, the spectro-polarimeter, and SFDI projection assembly. The system is composed of a Stokes imaging polarimeter with a 10-bit digital charge-coupled device (CCD) camera (Dalsa Genie, Billerica, MA) fixed at one scattering angle $\theta_s = 49$ degrees, which has been found optimal for the measurement of surface roughness [32]. Additionally, nine illumination tubes centered at $\theta_i = 49$ degrees are evenly distributed around the hemisphere. The choice of polar incidence angles was made simply by attempting to cover the hemisphere with the illumination ports, imaging arm and SFDI projection components. Each illumination tube contains a high performance white light-emitting diode (Cree, Durham, NC) followed by a polarizer ($P_1$ in Fig. 2) (Edmund Optics, Barrington, NJ), and a lens ($l_1$ in Fig. 2) (Edmund Optics, Barrington, NJ). Each illumination tube creates a semi-collimated 2 cm diameter beam with a fluence rate of approximately 2 Wcm$^{-2}$. Each light source is equipped with a built-in driver, which is controlled with a data acquisition module (DAQ) (National Instruments Corporation, Austin, TX). The spectro-polarimetric component of the system consists of two nematic liquid crystals variable retarders (LCR$_1$ and LCR$_2$ in Fig. 2) (Meadowlark Optics Inc., Frederick, CO), followed by a liquid crystal tunable filter (LCTF) (Meadowlark Optics Inc., Frederick, CO) with a built-in vertical polarizer ($P_2$ in Fig. 2). A LCTF was chosen instead of a filter wheel in order to give the system maximum versatility. The LCTF has a set range (450 to 700 nm with the full width at half maximum (FWHM) of 7 nm.

Because the sample plane is not parallel to the CCD plane ($l_2$ plane in Fig. 2), the image is only in focus along a line with coinciding sample and camera focal planes. This issue is rectified by tilting the camera relative to the lens with the angle of $\theta_s/2$ based on the Scheimpflug principle [33].
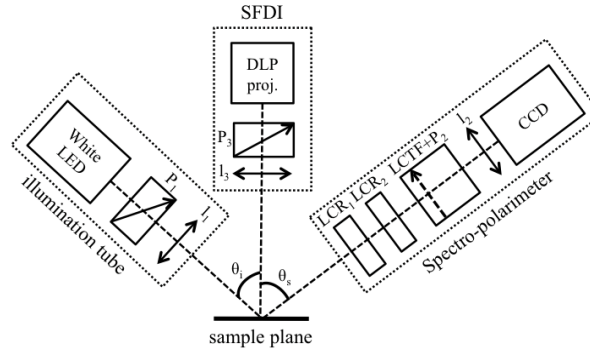


Fig. 2. A schematic side view of the polarized multispectral imaging system.

The out-of-plane scattering geometry is illustrated in Fig. 3, where $\theta_i$ and $\theta_s$ are the incident and scattering angles, respectively, and $\varphi_i$ is the incident azimuth angle. The out-of-plane Stokes polarimetry provides metrics sensitive to the surface roughness of a sample. Previous work has shown that backscattering of light due to roughness of a sample can be enhanced using the principal angle of polarization, $\eta$ [31]:

$$\eta = \frac{1}{2}\tan^{-1}\left(\frac{u}{q}\right).$$

(1)

where $u$ and $q$ are the Stokes vector components, $\mathbf{S} = [i\ q\ u\ v]$.
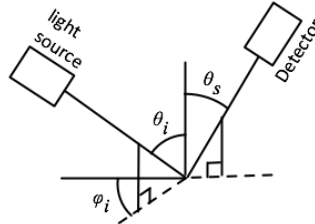


Fig. 3. The geometry of out-of-plane scattering; $\theta_i$ is the incident polar angle, $\theta_s$ is the scattered polar angle, and $\varphi_i$ is the incident azimuth angle.

SFDI [34] is a technique based on modulated illumination for the extrapolation of optical properties ($\mu_a$, $\mu_s'$) from a homogenous diffusive object, although recently extension to layered structures has been attempted [35]. In this work three two-dimensional sinusoidal patterns at different phases (0, $2\pi/3$, $4\pi/3$ radians) and specific spatial frequency were imposed on the sample and reflected light was captured using a camera. To determine optical properties of the sample at any wavelength of interest, the same set of three measurements on standard phantoms with known optical properties were provided with the same setup. Two-dimensional maps of absorption, $\mu_a$, and reduced scattering coefficients, $\mu_s'$, were reconstructed by applying the SFDI algorithm on the captured images, pixel by pixel. In this work the sample is treated as a single layered homogenous medium; this assumption has been made by other investigators [34] and it is appropriate for the shallow penetration depth used. The absorption coefficient maps at different wavelengths of interest were used to estimate the

volume fraction of tissue chromophores oxyhemoglobin, deoxyhemoglobin, melanin, and water based on the following equation:

$$\mu_a = B \times \left[ (1-S) \times \mu_{aHb} + S \times \mu_{aHbO_2} \right] + M \times \mu_{aMel} + W \times \mu_{aWater} + C. \qquad (2)$$

Where $\mu_a$ is the total absorption coefficient, $B$ is blood content, $S$ is oxygen saturation, $M$ is melanin content, $W$ is water content, and $C$ is a parameter used to mimic the spurious background absorption of tissue, which is generally close to 0. $\mu_{aHb}$, $\mu_{aHbO2}$, $\mu_{aMel}$ and $\mu_{aWater}$ are tabulated values of absorption coefficients of hemoglobin, oxyhemoglobin, melanin and water, respectively. A least-square fitting algorithm based on the Nelder-Mead simplex minimization method [36] was applied to the above equation to extrapolate the volume fraction of the various tissue chromophores. The reduced scattering coefficient maps were also analyzed to interpret the cellularity of examined tissue. As shown in Fig. 2, the SFDI imaging system was constructed as follows: a 200 ANSI Lumens DLP (Digital Light Processing) projector (ASUS P1 LED Projector) followed by a polarizer ($P_3$ in Fig. 2) (Edmund Optics, Barrington, NJ) and a lens ($l_3$ in Fig. 2) (Thorlabs, Newton, NJ) were added to the illumination port just above the hemispherical shell with normal direction to the sample. Specular reflectance from the sample was eliminated by adjusting the polarizer in front of the DLP projector ($P_3$ in Fig. 2) at 90 degrees with respect to the LCTF polarizer, ($P_2$ in Fig. 2). The imaging system for both modalities consists of a spectro-polarimeter and a fast acquisition CCD camera attached to a zoom lens ($l_2$ in Fig. 2) (Computar, Commack, NY). While utilizing SFDI, the effect of LCR cells was nulled to set zero retardance programmatically.

In this study, SFDI was run for 17 different wavelengths: 445, 500, 510, 529, 541, 545, 556, 560, 570, 577, 584, 588, 596, 620, 632, 650, and 670 nm. The range of porcine skin's optical properties at visible spectral range is reported by other groups: $\mu_a = 0.06 \sim 0.2$ mm$^{-1}$ and $\mu_s' = 1.0 \sim 2.5$ mm$^{-1}$ [37,38]. A value of spatial frequency $f_x = 1/3$ mm$^{-1}$ was chosen to obtain relatively shallow penetration depths. As Saager *et al.* [39] and Laughney *et al.* [40] noted at high spatial frequency the transport coefficient dominates these type of measurement and probing depths of less than 1 mm can be achieved for the visible-light range. The sinusoidal patterns were generated in Matlab and then transferred to the DLP system through a display mirroring approach.

Blood perfusion measurement was also conducted with a LDI system (Moor Instruments, Devon, UK). The system is non-contact and requires only a few seconds to generate a map of tissue perfusion in a relative unit of flux. The LDI data was processed with the accompanying Moor image-processing software (Moor Instruments, Devon, UK). To achieve better understanding of the pathophysiological changes seen in the experimental scar, the measurements obtained with the polarized multispectral imaging system were correlated with these perfusion data.

A reference suture was placed in each scar to aid in adjusting the imaging head of the multispectral system to recreate a consistent field of view from week to week. The field of view of the imaging head is a disc with approximate diameter of 25 mm. At every experimental time point, sets of control images from uninjured tissue were also collected with both the multispectral imaging and LDI systems. Considering reference points on the images, the mean and standard deviation of each chromophore were calculated for scars and uninjured skin at different time points from the same region of interest (approximately 8 mm x 8 mm). Statistical analysis of the LDI data was also conducted on the same region of interest considered for SFDI.

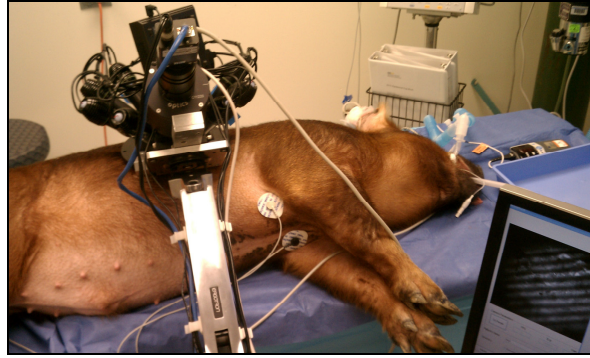An image of the complete system in the animal surgical suite is shown in Fig. 4.

Fig. 4. Polarized multispectral imaging system.

## 2.2 System calibration

The calibration of the imaging arm (Spectro-polarimeter) was performed by following a method that involved generating a set of known Stokes vectors and computing a data reduction matrix [41]. Figure 5 shows the calibration experimental set up. Thirty-six by six individual measurements were performed: $18 \times 6$ measurements *before* configuration, and $18 \times 6$ measurements *after* configuration. For each configuration, a computer-controlled rotary polarizer (Thorlabs, Newton, NJ) was placed in the illumination arm. This polarizer was tasked to rotate between 0 and 180 degrees, with steps of 10 degrees after each measurement. Retardation of each LCR was changed by feeding a set of six control voltages using LCR controller. Therefore, six individual readings were recorded by the CCD camera at each state of polarization of the incident beam.
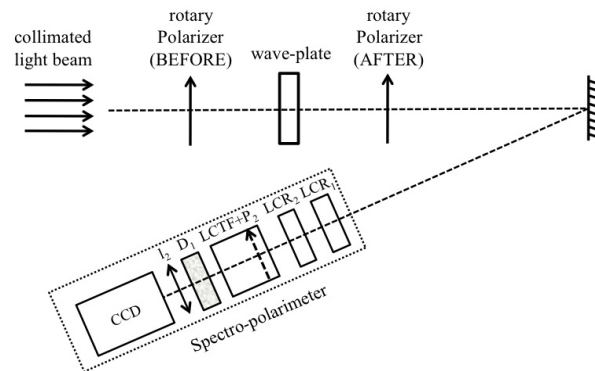


Fig. 5. Experimental set up for Spectro-polarimeter calibration; rotary polarizer was placed between light source and wave-plate for *before* configuration and between wave-plate and mirror for *after* configuration. $D_1$ shows the position of diffuser.

A diffuser ($D_1$ in Fig. 5) was placed before the camera lens ($l_2$ in Fig. 5) to create a uniform spot of light on the CCD array. The average of each image was calculated. By applying this calibration technique, a data reduction matrix, **W**, was reconstructed for each wavelength.

For each illumination tube the polarizer was set to 45 degrees from the incident plane formed by the tube and the sample [42]. A set of gold roughness samples was used to align these polarizers precisely. The principal angle of the polarization was calculated using the Stokes images captured from each gold standard at different azimuth angles. The data was also modeled using a facet scattering model from SCATMESH/MIST library (NIST, USA). A detailed explanation of the model is offered here [43] but briefly, the model treats a rough

object as a combination of random surface facets and a depolarizing scattering volume beneath the surface. The facet scattering model requires input parameters such as refractive index of the sample, polarization state of the incident light, wavelength, and the incident and scattered polar angles. The position of each illumination polarizer was adjusted until the best fit between the measurement and the model prediction was obtained.

Several phantom studies were completed to evaluate the efficacy of the SFDI module. The SFDI was tested using both absorbing and scattering flat polyurethane phantoms with known optical properties. Reduced scattering coefficient and absorption coefficient of phantoms were adjusted using Titanium dioxide and India ink respectively. A set of standard phantoms with different optical properties, some of them close to the $\mu_a$ and $\mu_s'$ of the experimental tissues, were selected. Results of the SFDI measurements were compared with the results done with an integrating sphere and Inverse Adding Doubling (IAD) [44].

*2.3 Porcine model of human hypertrophic scar*

A reproducible wound is paramount in the development of a model for the study of scar physiology. Considerable effort was dedicated to the development of a reliable wound yielding consistent and reproducible scar in this porcine model.

Controversy exists regarding the optimal model for the study of hypertrophic scar [45]. To study solely human tissues, the most ideal, is impractical due to uncontrollable factors such as timing from injury, depth of injury, and body location, especially in this preliminary work. Advantages of the use of a red Duroc pig include a relatively large size (adults can grow to 200kg) allowing for larger wounds and a flatter surface area than smaller mammals commonly used in scientific research like guinea pigs, rabbits, or rats. More importantly, it is well-documented that the skin of the Duroc pig exhibits similarities to humans in wound healing and scar formation on a molecular, cellular, and gross level [46–50].

To create hypertrophic scars, two excisional 100 mm by 100 mm full thickness wounds were created on the flanks of the animal with an electric dermatome (Zimmer Inc., Warsaw, IN) at a total dermatome depth of 2.3 mm, as previously described [51] (Fig. 6).
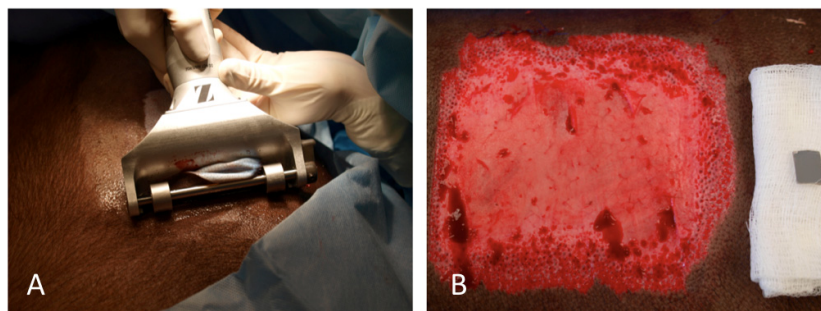


Fig. 6. Skin grafting using an electric dermatome (A) and excisional wound on day zero (B).

Every 7 days, the animal was anesthetized and wounds were evaluated by an experienced clinician in the operating room. Wounds were photographed, biopsied, and laser Doppler-imaged at each trip to the operating room, as detailed in Table 2, with weekly observations and imaging continuing for a total of 19 weeks. The wounds began reepithelialization from their edges and were completely closed between weeks 5 to 6. After reepithelialization had occurred, the VSS was incorporated into weekly examinations to subjectively assess healed wounds and their developing scars and the multispectral imaging process was initiated. On day 70, two weeks of compression therapy was begun, delivering 30mmHg of pressure to the experimental scars. A set of data obtained from one animal is shown in this report. The results of compression therapy are not presented in this paper.

**Table 2. Timing plan for the animal study**

| Time | Task |
|---|---|
| Day 0 | Creation of two wounds |
| Week 1-6 | Gross assessment (photograph, LDI and biopsy) |
| Day 49 | Starting polarized multispectral imaging |
| Day 70 | Starting compression therapy for two weeks |
| Weeks 13-19 | Continuing gross assessment and multispectral imaging |

## 3. Results and discussion

### 3.1 Calibration

The data reduction matrix, $W$, was achieved by applying the spectro-polarimeter's calibration procedure. Stokes parameters for a set of 38 incident polarized light with known states of polarization were calculated as $S_{4 \times 36} = W_{4 \times 6} \cdot I_{6 \times 36}$, where $I$ is the intensity matrix of the images, was captured by the CCD camera. Figure 7 shows the residual Stokes parameters (the Stokes measurement errors) obtained with the calibration technique at two wavelengths; $\lambda = 525$ and $632$ nm. The RMS of residues are 0.029 for $\lambda = 525$ nm and 0.019 for $\lambda = 632$ nm.
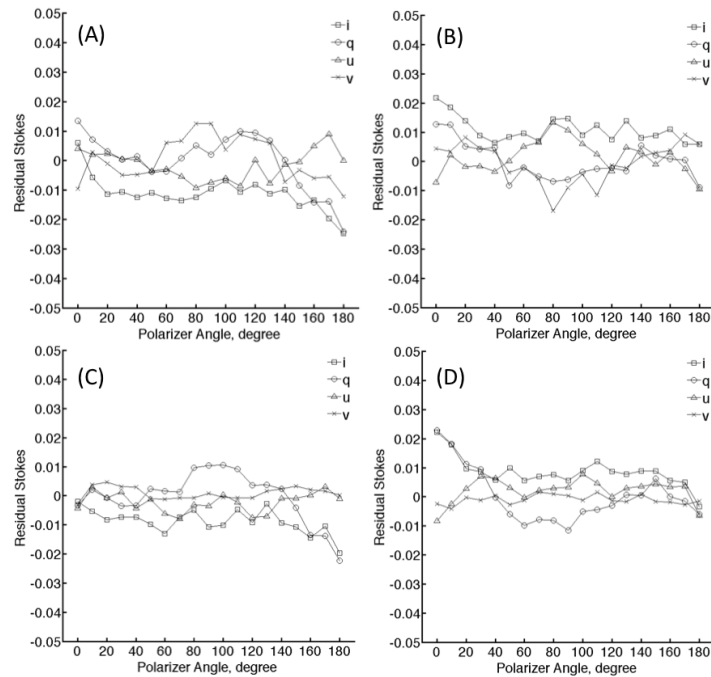


Fig. 7. Residual Stokes parameters for $\lambda = 525$ nm (A, B) $\lambda = 632$ nm (C, D) and as a function of the polarizer angle: A, C: *before*. B, D: *after*.

Five gold phantoms with different levels of roughness were imaged and the Stokes images at $\lambda = 632$ nm were formed for the nine illumination tubes. The mean value of the principle angle of the polarization ellipse, $\eta$, was calculated at each azimuth angle. With precise alignment of the state of polarization of each illumination tube, agreement between the model and the experimental results was achieved for all illumination angles (Fig. 8). Table 3 shows the RMS error between the experimental value of $\eta$ and the facet model prediction for each phantom. The total average RMS error was measured as 2.85 degrees.
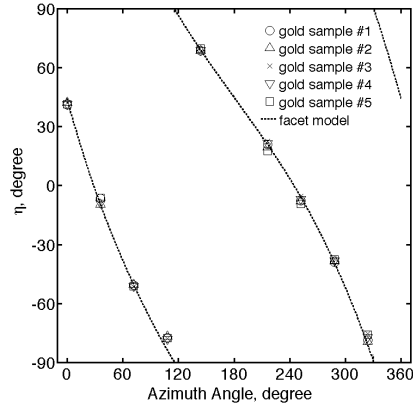
Fig. 8. The principal angle of polarization of gold samples for λ = 632 nm illumination from each of the tubes located at a different azimuth angles. There is a good agreement between measurements and the facet scattering model.

**Table 3. Gold roughness phantom - experimental RMS error**

|  | Gold sample | | | | |
|---|---|---|---|---|---|
|  | #1 | #2 | #3 | #4 | #5 |
| RMS error (degree) | 2.69 | 2.64 | 2.98 | 2.50 | 3.46 |

Figure 9 shows the calibration results of SFDI module for nine standard polyurethane phantoms at λ = 632 nm. Results showed an average error of 8.00% and 5.63% for the absorption coefficient and reduced scattering coefficient, respectively (average error < 10%). Figure 10 shows the optical properties of a single polyurethane phantom measured with the SFDI and IAD at 11 different wavelengths, λ = 455, 500, 510, 515, 529, 545, 556, 570, 584, 632, and 650 nm. The average error is 5.04% and 3.83% for absorption coefficient and reduced scattering coefficient, respectively.
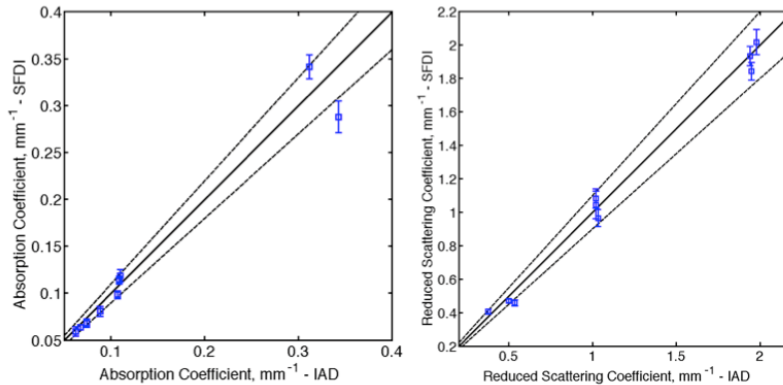


Fig. 9. Absorption and reduced scattering coefficient of polyurethane phantoms measured by the SFDI module versus the measurements by an IAD at λ = 632 nm. Rectangular symbols show the averaged value and error bars are the standard deviation of the data. Doted lines show ± 10% error boundaries.
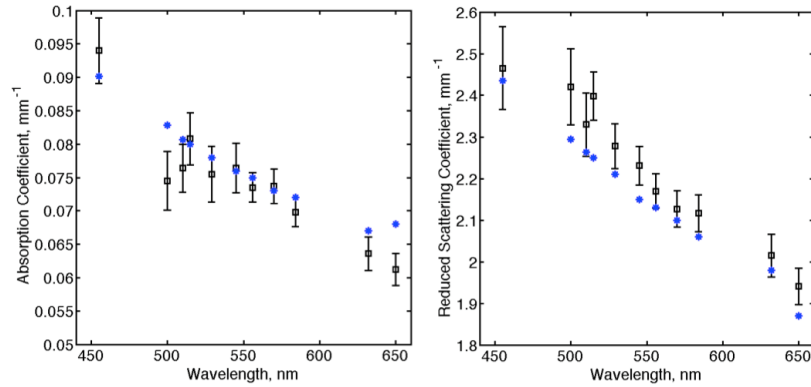
Fig. 10. Optical properties of a polyurethane phantom at various wavelengths. Rectangular symbols show the averaged value measured by the SFDI module and error bars are the standard deviation of the data. Asterisks show the measurements done by the IAD.

## 3.2 Spatial frequency domain imaging

To study the differences of tissue chromophores between the scars and normal tissue, maps of the optical properties of each scar were first reconstructed by applying the SFDI algorithm. The results show a variety of average optical properties at visible spectral range: $\mu_a = 0.04\sim0.2$ mm$^{-1}$ and $\mu_s' = 1.2\sim2.0$ mm$^{-1}$ for HTS and $\mu_a = 0.09\sim0.3$ mm$^{-1}$ and $\mu_s' = 0.9\sim1.4$ mm$^{-1}$ for uninjured skin tissue. Measurements were taken along 17 wavelengths and 13 time points. Using the minimization method shown in Eq. (2), maps of the tissue chromophores, including hemoglobin volume fraction ($B$ in Eq. (2), blood oxygenation level ($S$ in Eq. (2), water content ($W$ in Eq. (2), and melanin content ($M$ in Eq. (2) were extracted and analyzed. The volume fraction map of hemoglobin content (Hb) and oxygenation (SO$_2$) of a portion of a representative scar, as well as its digital photograph and perfusion map, are shown in Fig. 11.
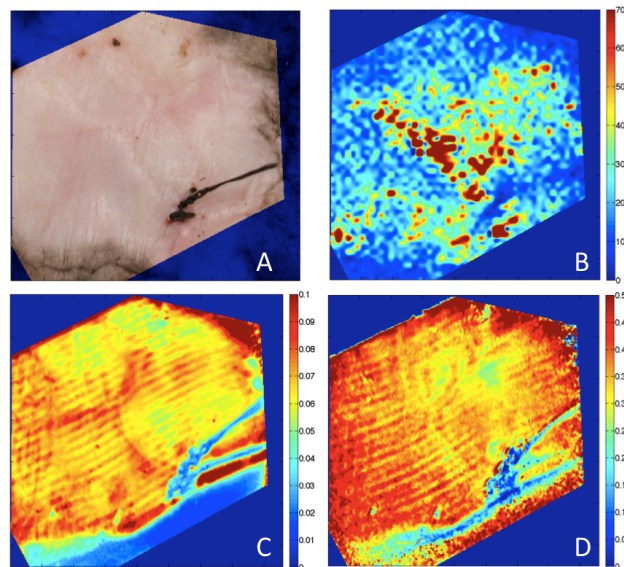


Fig. 11. Scar appearance on day 105 after wounding (A), scar's blood perfusion map (B), its Hb content (C) and SO$_2$ (D) maps. The black string visible in figure A shows the reference suture.

Figure 12(A) illustrates hemoglobin volume fraction values (B in Eq. (2) for two hypertrophic scars as well as uninjured control skin over time. Large changes in the blood content of each scar were seen between days 49 and 70 after wounding. This was expected for the fibroproliferative and reepithelialization phase of the wound healing. After reepithelialization was complete, wounds showed a trend toward decreased hemoglobin content. A decrease in blood hemoglobin content may have contributed to the wounds being less red. These findings were in agreement with the clinicians observation based on the VSS analysis, which is illustrated in Fig. 12(C). The VSS gross assessment showed that wounds went from red to pink in the surrounding time period of fibroproliferative and reepithelialization phase. The perfusion measurements obtained from LDI conducted in parallel with multispectral imaging are shown in Fig. 12(B). According to the results obtained from the SFDI and LDI techniques, the scarred tissue showed relatively higher level of static and dynamic blood content compared to uninjured skin. This is in agreement with clinician assessment of these scars as erythematous compared to the uninjured skin.

The metabolic activity of hypertrophic scar has been theorized to be higher than that of uninjured skin due in part to its active synthesis of collagen fibers [2]. This has been associated with a higher oxygen consumption rate as well [52, 53]. Indeed, results from this study showed that the blood oxygenation (S in Eq. (2) of hypertrophic scars was $41 \pm 2.3\%$ on average, compared to $50 \pm 2.3\%$ in uninjured skin.
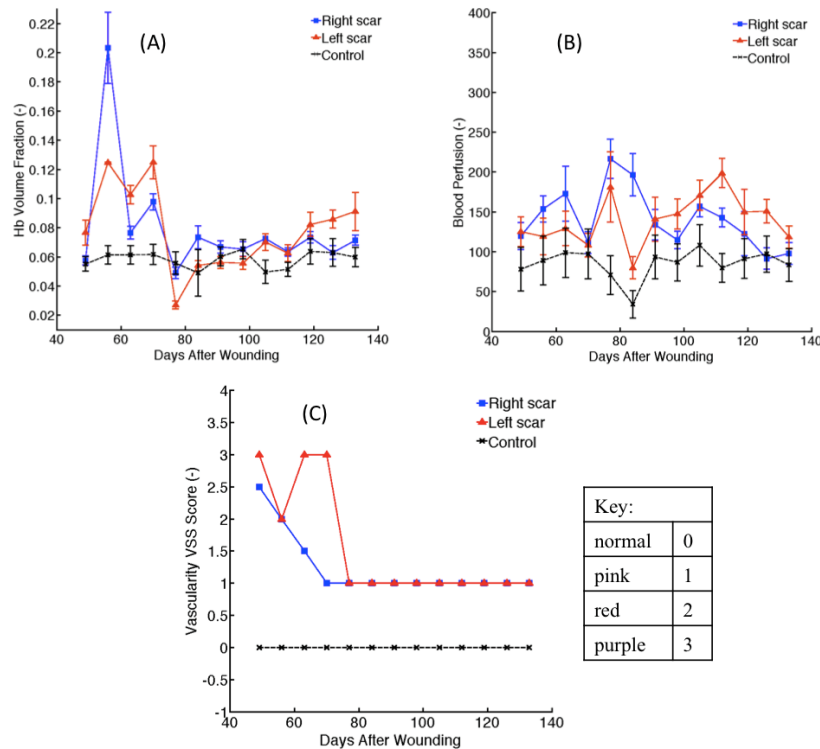


Fig. 12. Blood hemoglobin volume fraction versus time (A), blood perfusion versus time (B), and vascularity VSS score versus time (C). Control is uninjured skin.

Results of water content (W in Eq. (2) measurements using SFDI are presented in Fig. 13. This illustrates higher level of water content in scars (average W is 0.0013 for both right and left scars) compared to uninjured skin (average W is 0.0009).
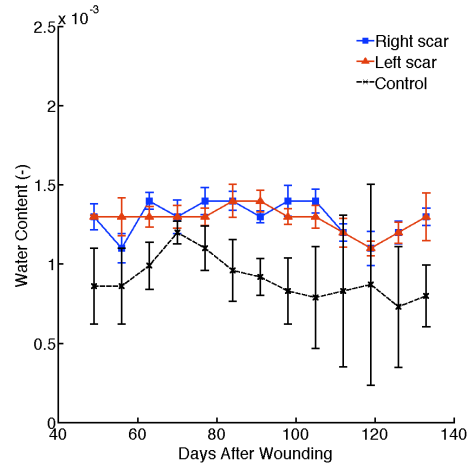
Fig. 13. Water content level versus time.

Scarring with abnormal pigmentation is a significant and disturbing outcome after thermal and other traumatic skin injuries [54]. Figure 14 shows melanin content ($M$ in Eq. (2) maps of hypo- and hyper-pigmented regions of a scar at two points in time; 70 and 126 days after wounding. These maps illustrate that hyper-pigmentation continued to increase in area and intensity. This specific scar showed the development of an island of hyper-pigmentation surrounded by hypo-pigmented skin. Figure 15(A) shows the trend in melanin concentration at several time points for both hyper- and hypo-pigmented regions of this scar. The baseline shows the average values of melanin content expected in normal uninjured skin. Scars were also detected and graded based on the VSS protocol (0 = normal, 1 = hypo-pigmentation, 2 = mixed-pigmentation, 3 = hyper-pigmentation). The pigmentation score on the VSS is the same for both scars at all time points; 2 = mixed-pigmentation (Fig. 15(B)). The scars are assessed as a whole in this system. Another advantage to using the proposed imaging system is that hyper- and hypo-pigmented scar samples can be examined separately, as shown below. Histological examination of punch biopsies taken from areas of hyper- and hypo-pigmentation and uninjured tissue were also performed. Consistent with the SFDI imaging, there is a clear increase in the amount of melanin staining of hyper-pigmented scar as compared to both the uninjured skin and the hypo-pigmented scar [55].
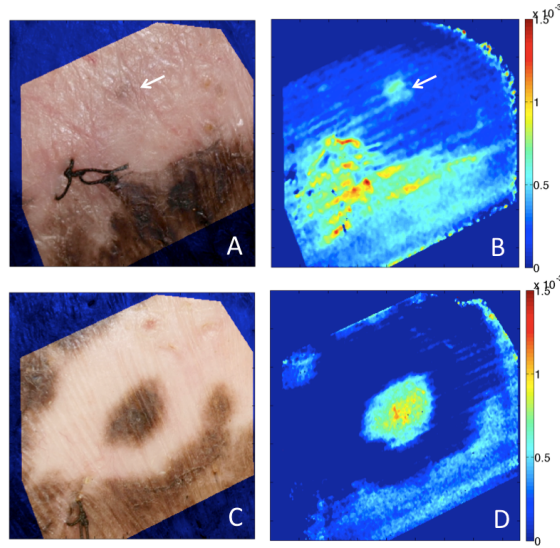
Fig. 14. Melanin volume fraction maps of the hyper- and hypo-pigmented regions of a scar on days 70 (A,B) and 126 (C,D).
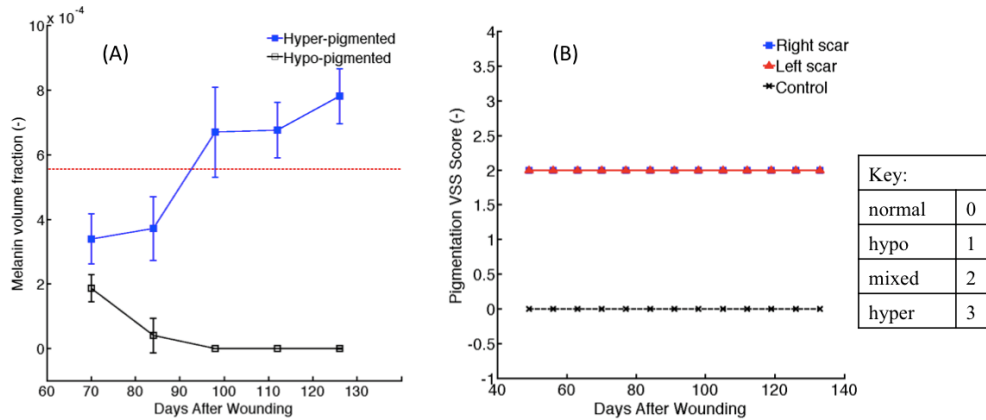


Fig. 15. Melanin volume fraction versus time (A) and pigmentation VSS score versus time (B). Control is uninjured skin

Hypertrophic scar formation usually results in a thickened skin with increased cellularity [28,29], which was also observed clinically in the scars under study in these experiments. Reduced scattering maps resulting from the SFDI technique revealed information relating to the scattering strength of tissue particles, potentially correlating with cell nuclei. Compared to uninjured skin, increased value of the reduced scattering coefficient of hypertrophic scar was seen, specifically at shorter wavelengths, where dominating Mie scattering from cylindrical collagen fibers is minimized, showed higher volume of cellularity which relevant histological reports are also noted in previous work. Figure 16 illustrates two maps of reduced scattering coefficient for normal skin (Fig. 16, left) and a representative scar (Fig. 16, right) at $\lambda$ = 455 nm. Figure 17 shows the reduced scattering values versus time for scar and uninjured skin at $\lambda$ = 455 nm.
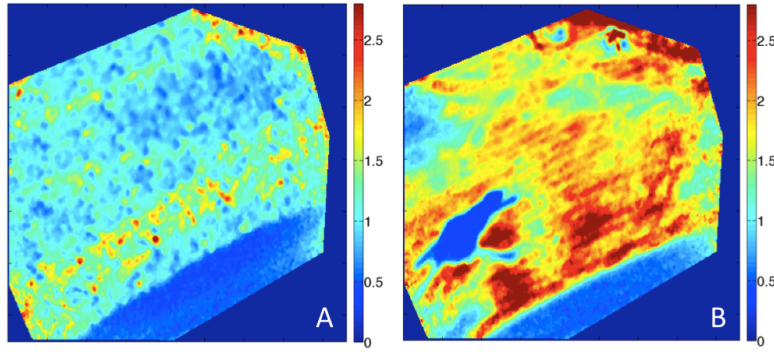
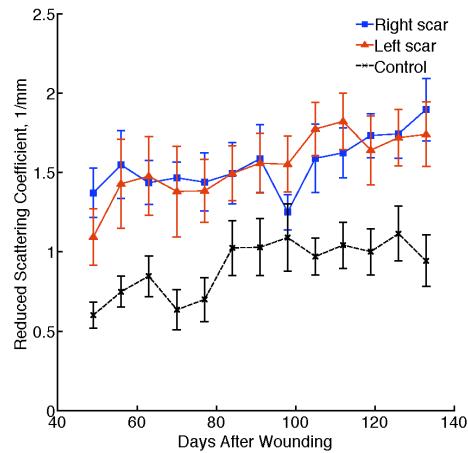Fig. 16. Reduced scattering coefficient maps at λ = 455 nm, normal skin (A) and HTS on day 119 after wounding (B).



Fig. 17. Reduced scattering coefficient versus time at λ = 455 nm.

## 3.3 Out-of-plane Stokes polarimetry

The texture and roughness of the surface of a scar is clinically relevant for patient comfort and cosmesis. To investigate changes in scar roughness, Stokes images were reconstructed from the spectro-polarimetric imaging data at λ = 525 nm and the deviation from the normal roughness, described as the polarized portion of the reflected beam, was obtained with the out-of-plane polarimetric imaging. Figure 18 shows a set of Stokes intensity images at two different time points during the course of the study. The principal angle of polarization, η, of targeted tissue was calculated from the Stokes images. Results for η at various time points are presented in Fig. 19 and compared with the facet analytical model. Analysis of the scars showed a tendency of the η to approach the rough surface facet model prediction as the scars matured.
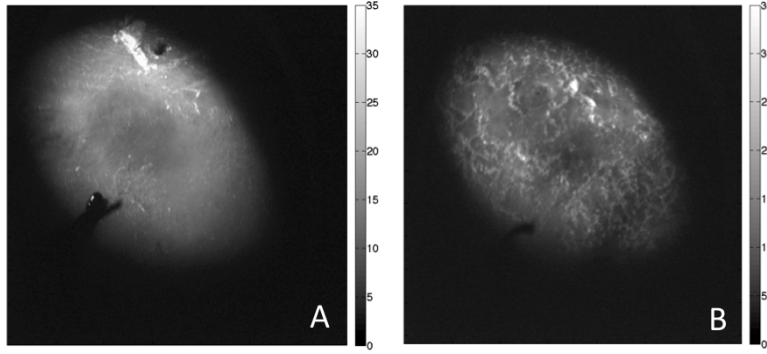
Fig. 18. Sample Stokes intensity images at λ = 525 nm captured at azimuth angles of 72 degrees from the same HTS on days 91 with shiny surface (A) and 112 with relatively rougher surface (B).
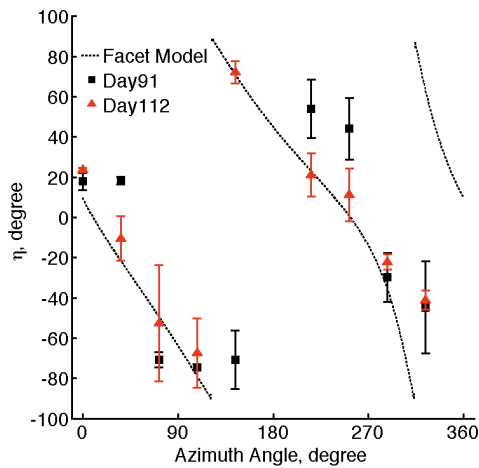


Fig. 19. The principal angle of polarization, $\eta$, versus azimuth angle at two points of time and λ = 525 nm. The dotted curve corresponds to the facet scattering model.

## 4. Conclusion

The multispectral imaging system was designed to evaluate quantifiable attributes hypertrophic scar quality and development. Results based on phantoms and some *in vivo* samples using a porcine model of human hypertrophic scar showed that the imaging system could provide information about the structural and functional properties of hypertrophic scars, which in many cases correlated with clinical observations. Vascularity, pigmentation, water content, and cellularity of examined scars were estimated with SFDI and showed clinical correlations by gross and histologic examination.

This new imaging system has several advantages compared to current methodologies. It is non-contact and non-invasive, and thus can be used at any stage in wound healing without causing discomfort or additional injury to the patient. Pigmentation, hemoglobin, water and polarization assessments are co-registered and are based on imaging rather than point measurements, allowing for more meaningful interpretation of data. Furthermore new metrics such as localized pigmentation versus the current VSS interpretation of global scar color may be more relevant when assessing a scar as we have shown in Fig. 15. For this particular scar the clinician interpretation of VSS remained at 2 (mixed pigmentation) while with our methodology we were able to show that specific areas of the wound became hyper-pigmented over time.

Water content remained elevated in both scars compare to normal non-injured skin. This finding agrees with previous studies on hypertrophic scars using OCT [56]. An increase in hypertrophic scars' water content may be attributed to increased concentrations of glycosaminoglycan sugar chains in the extracellular matrix, which notably attract water [57]. Our method of measuring roughness utilizes polarimetric techniques and specifically the principal angle of polarization. This metric is independent from optical properties, as we have previously demonstrated [31], and for this reason particularly suited to this environment.

We acknowledge that using SFDI within an animal model framework has its limitations. Although the animals imaged were sedated respiratory movement and other motion impacted the measures at times, when possible the measurement was repeated to obtain more reliable data. Furthermore as Bodenschatz et al. have pointed out *Height Adjustment Errors* [58] may arise when the distance between camera and sample changes, as it could occur in deep wound studies. This error leads to an underestimation of the absorption coefficient and increase in scattering coefficient and may explain some of the variability in our data.

Ultimately, this device, taken together with these results, may lead to a complementary, noninvasive technique for scar evaluation to pair with the subjective evaluation of experienced clinicians. Ideally, hypertrophic scar may be detected earlier in development allowing for earlier therapeutic intervention [59]. To truly generalize the findings presented here, further studies on an increased sample size are necessary to support and confirm these preliminary data.

**Acknowledgment**